https://doi.org/10.3311/PPch.39741

Periodica Polytechnica Chemical Engineering, 69(2), pp. 173–190, 2025

SCAPS Modeling and Improvement of the Characteristics of Cu/ZnO/P3HT/Pt Hybrid Solar Cells with Inorganic Electron Transport Layer

Lina Merzougui[1,2], Mostefa Benhaliliba[2*], Sagar Bhattarai[3,4]

[1] Department of Energetic, Faculty of Physics, University of USTOMB, 31130 El Mnaouar, Oran, P.O.B. 1505, Algeria
[2] Film Device Fabrication-Characterization and Application FDFCA Research Group USTOMB, 31130 El Mnaouar, Oran, P.O.B. 1505, Algeria
[3] Technology Innovation and Development Foundation, Indian Institute of Technology Guwahati, 4th Floor, Research Building, 781039 Guwahati, Assam, India
[4] Centre for Research Impact & Outcome, Chitkara University Institute of Engineering and Technology, Chitkara University, 140401 Rajpura, Punjab, India
* Corresponding author, e-mail: mostefa.benhaliliba@univ-usto.dz

Received: 29 December 2024, Accepted: 07 May 2025, Published online: 10 June 2025

Abstract

This study presents a thorough optimization approach for Cu/ZnO/P3HT/Pt hybrid solar cells (HSCs), providing insights into the interactions of several crucial parameters. Significant performance improvements are attained by carefully adjusting the absorber and electron transport layer (ETL). Enhancement of open-circuit voltage (V_{oc}) and reduction in recombination represent principal mechanisms by which precise aluminum doping in ZnO contributes to increased power conversion efficiency (PCE). In our simulations, an aluminum doping concentration of 4% in ZnO, an ETL thickness optimized at 0.004 µm, and an electron affinity set to 4.25 eV (the energy released when an electron binds to a neutral atom or molecule) together improve the PCE.

A critical finding is the identification of an optimal absorber layer thickness (2.5 µm), which achieves a maximum PCE of 16.82%. An examination of the interface fault density revealed a critical threshold of 10^{13} 1/cm^2, above which the performance started to decline quickly. The ideal operating point is found to be 313 K based on temperature-dependent research, with a peak PCE of 17.13%. Integrating advanced current-voltage characterization, innovative band alignment studies, and comprehensive temperature-dependent analyses, this work advances the theoretical framework for optimizing HSCs.

This research opens new avenues for the rational design of high-efficiency photovoltaics and highlights the transformative potential of multiparameter optimization and interface engineering in next-generation solar technologies.

Keywords

Al-doped ZnO (AZO), hybrid solar cell, ETL, poly(3-hexylthiophene (P3HT), electron affinity, impedance

1 Introduction

Hybrid solar cells (HSCs) integrate the flexibility and cost-effectiveness of organic semiconductors like poly(3-hexylthiophene) (P3HT, a light-absorbing polymer) with the stability and high carrier mobility of inorganic zinc oxide, offering a sustainable alternative to conventional photovoltaics. While third-generation technologies such as perovskite solar cells exhibit high efficiencies, their adoption is limited by toxicity, scalability challenges, and environmental instability [1]. In contrast, Cu/ZnO/P3HT/Pt-based HSCs leverage the tunable optoelectronic properties of P3HT [2, 3] and robust charge transport of ZnO [4, 5] presenting a viable path forward. However, critical challenges impede their performance as the low open-circuit voltage (V_{OC}) due to recombination losses at the ZnO/P3HT interface [6], suboptimal electron transport layer (ETL) design, where uncontrolled aluminum doping and thickness variations degrade charge extraction [7, 8] and the thermal instability, causing efficiency decline at elevated temperatures.

Prior studies have addressed individual challenges, such as Al doping enhancing ZnO conductivity [8] and ultra-thin aluminum doping in ZnO (Al-doped ZnO or AZO)

Cite this article as: Merzougui, L., Benhaliliba, M., Bhattarai, S. "SCAPS Modeling and Improvement of the Characteristics of Cu/ZnO/P3HT/Pt Hybrid Solar Cells with Inorganic Electron Transport Layer", Periodica Polytechnica Chemical Engineering, 69(2), pp. 173–190, 2025. https://doi.org/10.3311/PPch.39741

layers improving transparency [9]. However, a holistic analysis of multiparameter interactions Al doping concentration, ETL thickness, electron affinity (energy required to remove an electron from a material), and temperature remains unexplored. For instance, excessive Al doping introduces defects [8], while overly thin ETLs risk incomplete charge extraction [9].

This study bridges this gap through solar cell capacitance simulator (SCAPS-1D, a numerical tool for modeling photovoltaic devices) simulations of the Cu/ZnO/P3HT/Pt architecture, with three objectives: first, optimizing Al doping in ZnO to balance enhanced electrical conductivity with defect suppression, thereby minimizing recombination losses; second, establishing design rules for ETL thickness and electron affinity to maximize charge extraction efficiency while mitigating optical losses; and third, resolving temperature-driven performance compromises to identify operational thresholds that ensure stability under real-world conditions.

This approach addresses the growing demand for sustainable and scalable photovoltaics. The simulations, performed using SCAPS-1D, achieved a 17.13% power conversion efficiency (PCE), a 73% improvement over undoped devices. This enhancement can be attributed to a complex interplay of factors, primarily the reduction in Shockley-Read-Hall (SRH) recombination and improved band alignment at the AZO/P3HT interface. Theoretically, SRH recombination, a dominant loss mechanism in solar cells, is reduced by Al doping in ZnO, which passivates defect states within the ZnO lattice and potentially shifts the Fermi level, decreasing the probability of trap-assisted recombination events, while defining critical thresholds for interface defects (<10^{13} 1/cm^2) and temperature (313 K). These findings advance the theoretical framework of hybrid interfaces and provide practical strategies for developing efficient, stable HSCs with real-world applicability.

Definitions of all symbols and abbreviations used in this paper are collected in the Nomenclature, which appears just before the References.

2 Device structure and simulation methodology

For analyzing thin-film solar cell performance, researchers can choose from several computational platforms. While tools like SILVACO ATLAS, AMPS, PC1D, AMPS [10], and COMSOL [11] are available. Here, SCAPS-1D version 3.3.10 [12], for device modeling is used. This software platform, created by Burgelman et al. [13] at the University of Ghent, offers comprehensive one-dimensional simulation capabilities. The program's ability to model up to seven distinct layers in photovoltaic structures makes it particularly adaptable for diverse solar cell configurations. Its reliability has been confirmed through numerous experimental validations, establishing it as a dependable platform for solar cell performance analysis [14].

The fundamental physics of semiconductors, encompassing both Poisson's equation and charge carrier continuity equations, forms the mathematical foundation of SCAPS-1D's computational approach. Through these principles, the software generates comprehensive alternating current (AC) and direct current (DC) electrical behavior simulations [15]. These equations control important processes that are essential to comprehending how photovoltaic devices behave, including charge production, recombination, and transport.

The mathematical framework begins with Poisson's differential equation:

$$div\left(\varepsilon\nabla\psi\right)=-\rho, \tag{1}$$

where ε is the material permittivity, ψ is the electric potential and ρ is the volumetric charge density.

Following Eq. (1), the conservation of charge carriers is expressed through the continuity equations for both electrons and holes, which can be represented as:

$$\frac{\partial n}{\partial t}=\frac{1}{q}div\overrightarrow{j_n}+GE_n-RE_n, \tag{2}$$

$$\frac{\partial p}{\partial t}=\frac{1}{q}div\overrightarrow{j_p}+GE_p-RE_p. \tag{3}$$

In Eqs. (2) and (3), t is for time, q is the elementary charge (1.602×10^{-19} C), the carrier distribution is characterized by n and p, which indicate electron and hole concentrations, respectively. The movement of these carriers is quantified through their current densities, expressed as $\overrightarrow{j_n}$ for electrons and $\overrightarrow{j_p}$ for holes. The dynamic processes of carrier creation and loss are represented by generation rates (GE_n, GE_p) and recombination rates (RE_n, RE_p) for each carrier type.

The Cu/ZnO/P3HT/Pt HSC architecture integrates organic and inorganic materials to leverage their complementary optoelectronic properties. Below, the structure (Fig. 1) and utility of each material are detailed:

- Copper: front contact: metallic layer with high electrical conductivity (~5.96×10^5 S/cm) and a work

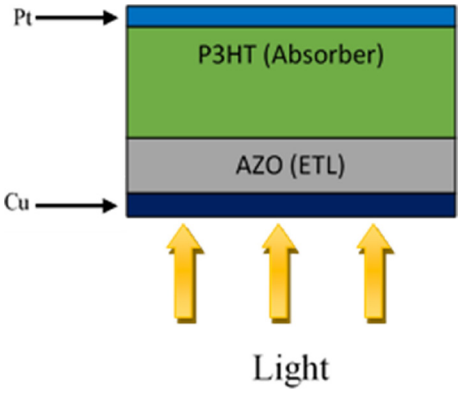

Fig. 1 Schematic representation of the hybrid organic-inorganic solar cell structure (Cu/AZO/P3HT/Pt)

function of ~4.7 eV, serves as the anode, collecting holes generated in the absorber layer (P3HT) and transporting them to the external circuit [16].

Copper is cost-effective compared to noble metals like Au or Ag and provides low series resistance, ensuring efficient charge extraction [17, 18].

- Aluminum-doped zinc oxide (AZO): ETL: *n*-type inorganic semiconductor, doping ZnO with Al increases carrier concentration and conductivity while maintaining optical transparency [19].

  It is used to extract electrons from the absorber (P3HT) to the front contact (Cu) and blocks holes, reducing recombination.

  Al doping enhances ZnO's conductivity by introducing oxygen vacancies and free electrons, while ultrathin layers mitigate optical losses [20, 21].
- P3HT: absorber layer: *p*-type organic polymer with a bandgap of 1.7 eV, absorption coefficient >10^5 1/cm in the visible spectrum, and hole mobility ~2×10^{-4} 1/cm^2/Vs [22–25].

  It is used to absorb photons and generate excitons, which dissociate at the AZO/P3HT interface into free carriers.

  P3HT offers solution processability, flexibility, and defect tolerance compared to inorganic absorbers like Sb_2S_3 or perovskites [22].
- Platinum: back contact: noble metal with a high work function (~5.6 eV) and stability under ambient conditions [26].

  Acts as the cathode, collecting electrons from the ETL (AZO) and completing the circuit. Platinum's inertness prevents oxidation, ensuring long-term device stability, while its high conductivity minimizes contact resistance [26].
- AZO/P3HT interface: a defect density <10^{13} 1/cm^2 is critical to suppress SRH recombination. Higher defect densities degrade PCE due to trap-assisted recombination [27, 28].
- Band alignment: the conduction band offset between AZO (3.95 eV) and P3HT (3.9 eV) facilitates electron injection while blocking holes, enhancing charge separation [29].

The simulation using SCAPS-1D employed ohmic boundary conditions at both front and back contacts, with work functions aligned to Cu (4.7 eV) and Pt (5.6 eV) respectively. SRH recombination mechanisms at the AZO/P3HT interface were modeled using variable defect densities (N_t) ranging from 1010 to 10^{16} 1/cm^2, with energy levels distributed across the bandgap to accurately represent the heterojunction interface dynamics.

An overview of the key parameters used in the device simulation is shown in Table 1, drawn from the current

Table 1 Material properties utilized for the simulation

Material properties	ZnO: 0% Al doping	ZnO: 2% Al doping	ZnO: 3% Al doping	ZnO: 4% Al doping	P3HT
Thickness (µm)	0.05	0.05	0.05	0.05	0.8 (varied)
Band gap (eV)	3.332	3.429	3.458	3.5	1.7
Electron affinity (eV)	4.029	3.99	3.983	3.95	3.9
Dielectric permittivity	9	9	9	9	3.0
Conduction band (CB) effective density of states (DOS) (1/cm^3)	3.040E17	6.040E18	2.52E19	5.5E19	1.0E20
Valence band (VB) effective DOS (1/cm^3)	4.576E19	4.476E19	4.476E19	4.476E19	1.0E20
Electron mobility (cm^2/Vs)	7.9E1	8.5E1	1.29E2	1.275E2	2.0E1
Hole mobility (cm^2/Vs)	6.1E1	7E1	9E1	6.725E1	2.0E1
Donor density (N_D) (1/cm^3)	1.25E13	1.3E17	9.5E17	5E18	0
Acceptor density (N_A) (1/cm^3)	0	0	0	0	1.0E15

literature [30–33] and experimental data [34]. All simulations are conducted under standard AM1.5 irradiation conditions, with an operational temperature of 300 K (except when studying the effects of varying temperatures).

3 Results and discussion

3.1 Effect of aluminum doping on ZnO

The incorporation of aluminum dopants into ZnO produces multiple beneficial modifications to the material's properties. This doping process enhances the interfacial stability between ZnO and the absorber layer through fundamental property alterations. Additionally, the aluminum incorporation significantly enhances both the density of charge carriers and electronic transport capabilities within the material [7, 35, 36].

Fig. 2 illustrates how doping ZnO with Al affects the V_{OC} and short-circuit current density (J_{SC}) characteristics of a ZnO/P3HT HSC.

V_{OC} increases significantly, from approximately 0.98 V for undoped ZnO to 1.08 V for 3% of doping, this growth can be ascribed to the enhancement in the conductivity of ZnO due to Al doping, Al doping enhances ZnO conductivity by substituting Zn^{2+} with Al^{3+}, increasing free electron density. This reduces recombination losses by shifting the Fermi level closer to the conduction band, improving charge separation [37].

There is a slight decrease in V_{OC} between 3 and 4% doping, suggesting a saturation effect or deterioration of the crystalline structure at higher doping levels. Excessive doping introduces lattice strain and defects, increasing trap-assisted recombination and offsetting conductivity gains.

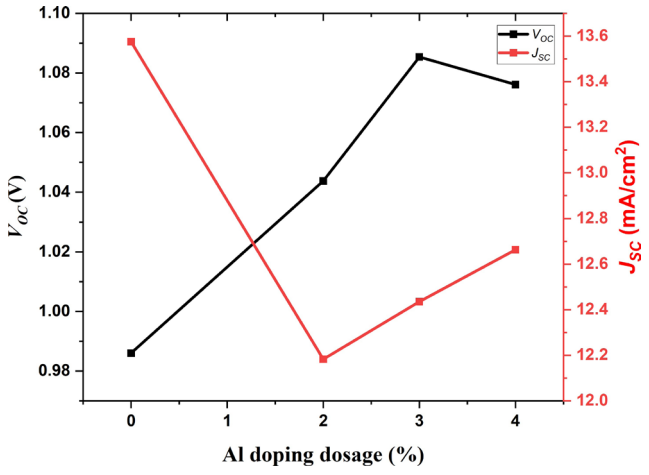

Fig. 2 Effect of aluminum doping on open-circuit voltage V_{OC} (maximum voltage) and J_{SC} (current under zero resistance) of ZnO/P3HT HSCs

The J_{SC} indicates a nonlinear trend, it significantly decreases from 0% to 2% of doping (from 13.6 to 12.2 mA/cm^2), then it increases slightly from 2% to 4% of doping (from 12.43 to 12.66 mA/cm^2). The initial decrease in J_{SC} may be due to a reduction in light absorption caused by the expansion of the band gap of ZnO doped (3.332 eV for pure ZnO, 3.429 eV for 2% doped-ZnO, 3.458 eV for 3% doped-ZnO and 3.5 eV for 4% doped-ZnO). The subsequent increase in J_{SC} at higher doping levels can be attributed to better load collection through improved conductivity.

Fig. 3 displays the impact of aluminum doping on fill factor (FF) and PCE of the ZnO/P3HTHSC. The FF rises significantly from 0% to 2% doping (from ~74% to ~86%). Highest values are attained at 2% doping. Beyond 2%, the FF decreased slightly, stabilizing at approximately 83–84% for 3% and 4% doping. The initial increase in FF indicates an improvement in junction quality and charge transport with Al doping. The slight decrease in the FF after 2% could be due to the saturation of the beneficial effects of doping or the emergence of negative effects at higher concentrations.

The PCE exhibited a steady increase with the Al doping. It increased from approximately 9.9% for the undoped ZnO to approximately 11.4% with 4% doping.

The increase in PCE aligns well with the increase in V_{OC} observed in the previous curve. The slight decrease in FF after 2% could be related to the initial decrease in J_{SC}; however, it is offset by the continued increase in V_{OC}.

The findings of this study on Al doping's impact on ZnO align with previous research in the field. For instance, they demonstrated that incorporating aluminum into ZnO enhanced the PCE of perovskite solar cells from 10.8% to 12.0% [38]. The validity of the findings is supported

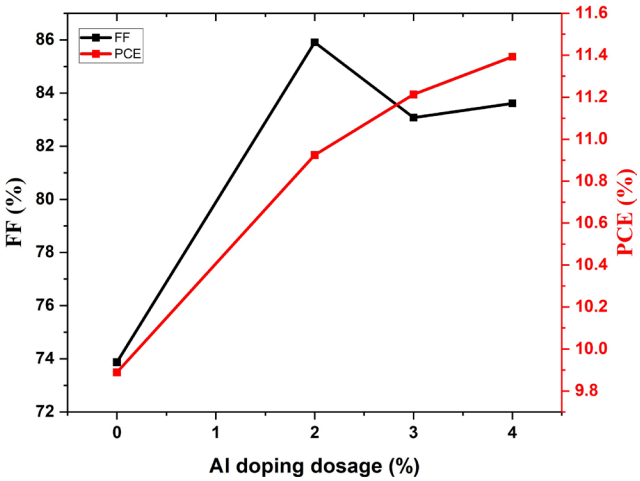

Fig. 3 Effect of Al-doping on the FF and PCE of ZnO/P3HT HSCs

by the uniformity of doping impact on electrical and optical characteristics across several investigations. In a different study, they fabricated Al-doped ZnO substrates using radio frequency (RF) sputtering. Their findings revealed that these substrates achieved electrical and optical performances similar to those of commercial indium tin oxide (ITO), with solar cells reaching PCE of approximately 10% under standard illumination conditions [39]. These parallel outcomes from independent studies further support the observations of the beneficial effects of Al doping in ZnO for solar-cell applications.

Furthermore, simulation results are contrasted with experimental and simulation data for the poly(3-hexylthiophene) blended with [6,6]-phenyl-C_{61}-butyric acid methyl ester (P3HT:PCBM) and the donor polymer J71 blended with the non-fullerene acceptor 1,1-dicyanomethylene-3-indanone-based small molecule 3,9-bis(2-methylene-(3-(1,1-dicyanomethylene)-indanone))-5,5,11,11-tetrakis(4-hexylphenyl)-dithieno[2,3-d:2′,3′-d′]-s-indaceno[1,2-b:5,6-b′]dithiophene (m-ITIC) (J71:m-ITIC) systems that have been published in the literature [34]. For P3HT:PCBM system, simulations showed a trend similar to that observed experimentally, with improved cell performance upon Al doping with ZnO. However, simulations indicate a more pronounced improvement for 3% Al doping (V_{OC} increase from 0.98 V to 1.08 V), whereas previous experimental studies [34] on P3HT:PCBM systems showed optimal performance at 3% doping with a V_{OC} increase from 0.95 V to 1.02 V. This discrepancy may arise from differences in interface defect densities (assumed as 10^{13} 1/cm^2 in simulations and more than 10^{14} 1/cm^2 in experimental devices [34]) or variations in morphological homogeneity during fabrication. Similarly, for the J71:m-ITIC system, simulations predicted a continuous J_{SC} improvement up to 4% doping, while experimental work [30] reported peak of J_{SC} at 2% doping (14.1 mA/cm^2 for experimental work and 12.66 mA/cm^2 for simulations), likely due to unaccounted carrier trapping in thicker doped layers. These differences between the simulations and experimental data highlight the complexity of the interfacial interactions and the importance of morphological effects. Nevertheless, the general trend of performance improvement with Al doping of ZnO is consistent between our simulations and literature results.

Fig. 4 depicts the total recombination current density (J_{TOTrec}) as a function of the applied voltage for different Al doping levels in ZnO, which provides crucial insights into the impact of doping on solar cell performance.

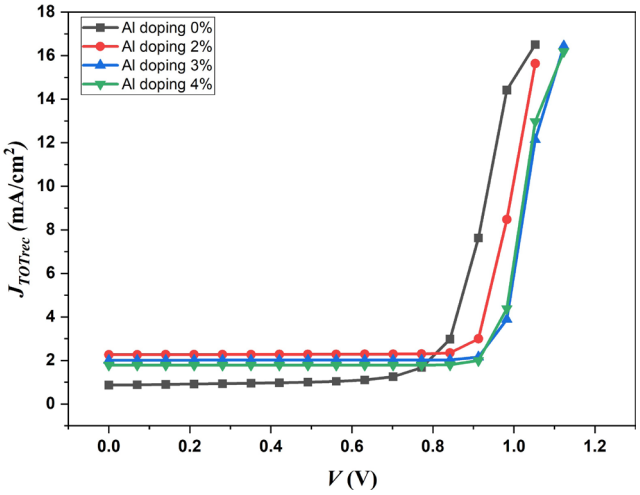

Fig. 4 Effect of ZnO doping on total recombination current density

Examining this curve in two distinct voltage ranges reveals the underlying mechanisms affecting cell efficiency.

From 0 V to 0.8 V, we observe that 2% doping slightly increases the recombination current compared to the undoped ZnO, while 3% and 4% doping significantly reduce This explains the initial slight decrease in J_{SC} at 2% doping and the subsequent increase at higher doping levels.

In the 0.8 V to 1.2 V range, all curves sketch a rapid increase in recombination current, but doped samples exhibit a delayed and less pronounced increase. This shift towards higher voltages for the onset of strong recombination explains the significant increase in V_{OC} with doping.

These observations justify the non-monotonic trend in J_{SC}, continuous increase in V_{OC}, improvement in FF (at 2% doping), and overall enhancement in PCE with increasing doping levels. The recombination curve analysis highlights the critical role of Al doping in reducing recombination, Al passivates oxygen vacancies in ZnO, suppressing defect states responsible for SRH recombination. At 4% doping, recombination minima correlate with optimal defect passivation and band alignment, leading to an overall improvement in solar cell performance.

This study underscores the importance of fine-tuning the doping level to maximize the benefits while minimizing the potential negative effects, offering a comprehensive explanation of the performance trends observed in previous J_{SC}, V_{OC}, FF, and PCE curves. This indicates that deliberately altering the recombination processes across various voltage ranges by appropriate Al doping of ZnO is a successful method for increasing the efficiency of HSCs.

The study of the various recombination current density curves, as shown in Fig. 5, J_{SRH} (Shockley-Read-Hall),

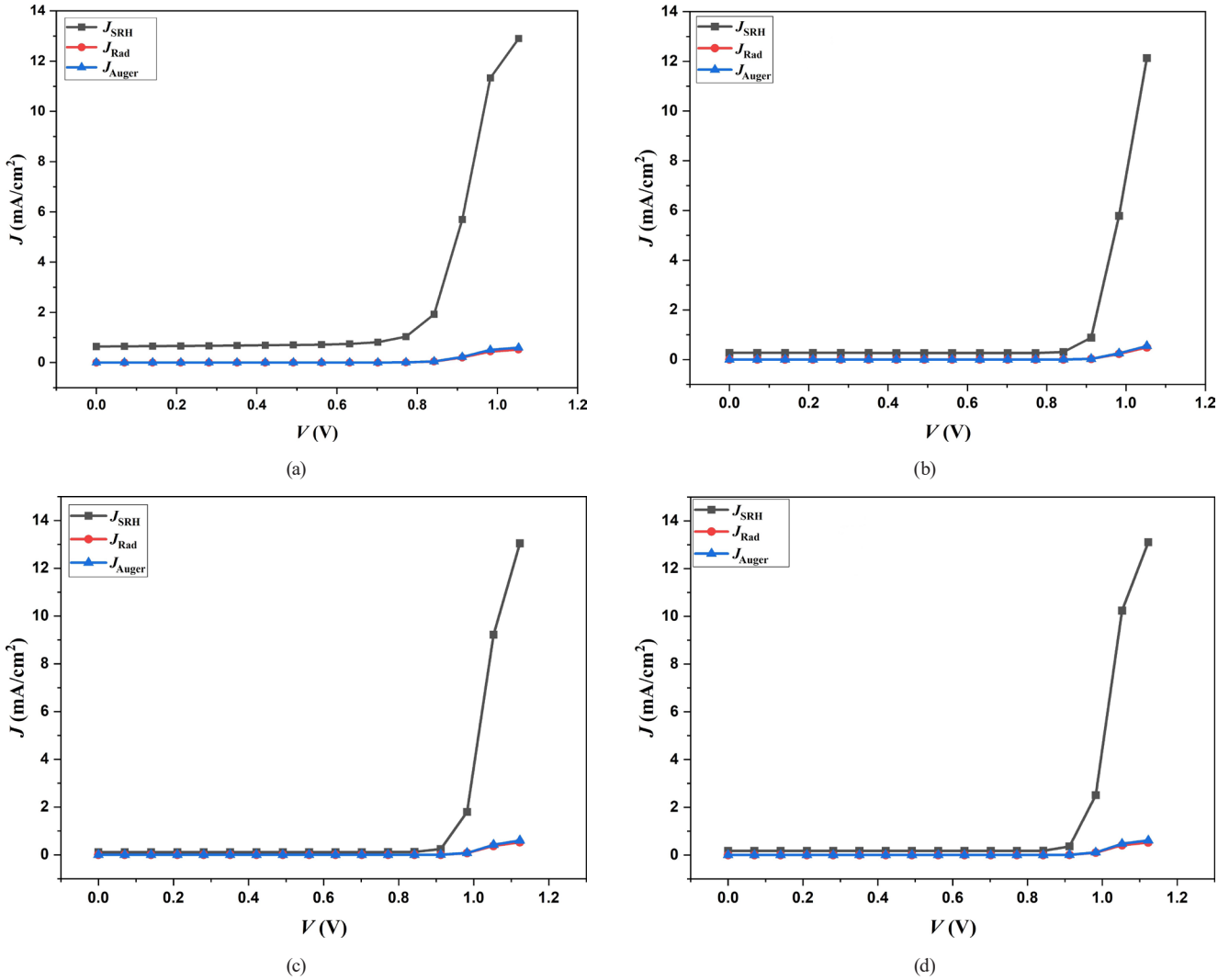

Fig. 5 Comparative analysis of SRH, radiative, and Auger recombination mechanisms in ZnO/P3HT HSCs at varying aluminum doping levels: (a) 0% doping; (b) 2% doping; (c) 3% doping; (d) 4% doping

J_{Rad} (radiative), and J_{Auger} (Auger)) as a function of the applied voltage for different doping levels of ZnO is essential for understanding the recombination mechanisms in ZnO/P3HT HSC. This analysis allowed us to identify the dominant loss processes and to evaluate the specific impact of doping on each type of recombination.

The results indicate that SRH recombination (J_{SRH}) is dominant at all voltages, particularly at high voltages, and it decreases significantly with increasing doping. Undoped ZnO exhibits high defect density, leading to SRH-dominated losses. Al doping reduces trap density, lowering SRH recombination. Radiative recombination, although low at all voltages, showed a slight increase with doping, especially at high voltages, likely owing to an improvement in the crystalline quality of ZnO, which promoted band-to-band recombination. Auger recombination is negligible at low voltages, but becomes more significant at high voltages, increasing slightly with doping. This increase is consistent with a higher carrier concentration, which favors this type of three-particle recombination.

Fig. 6 displays the Shockley-Read-Hall recombination current density against bias voltage (V) for various levels of Al doping in the ZnO/P3HT HSC. This curve isolates the effect of Al doping on the SRH mechanism, allowing us to understand how doping influences the most significant loss mechanism in HSC. The analysis shows that for all doping concentrations, J_{SRH} remains low at low voltages and increases rapidly at higher voltages, with a significant reduction observed owing to Al doping. In the absence of doping (0% Al), the J_{SRH} is the highest, whereas at 2% Al, a notable decrease in the J_{SRH} is observed. This reduction became even more pronounced at Al concentrations of 3% and 4%, although the curves are very close, suggesting a saturation effect.

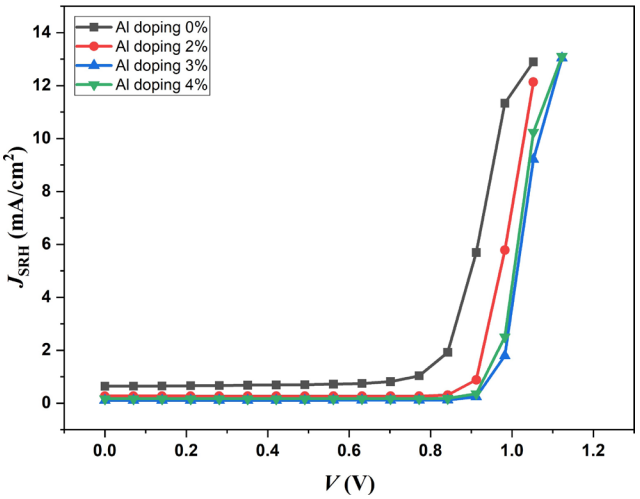

Fig. 6 Effect of Al-doping on J_{SRH}–V characteristics

The voltage region analysis reveals that at low voltage (0–0.6 V), J_{SRH} remains low and stable for all doping levels, whereas at medium voltage (0.6–0.8 V), it begins to increase, especially for undoped ZnO. At high voltages (>0.8 V), J_{SRH} increased rapidly for all doping levels; however, the magnitude of the increase varied with Al concentration. This reduction in J_{SRH} with Al doping suggests a decrease in the effective density of trap states or a modification of their energy distribution, contributing to a better collection of photogenerated charges, thereby justifying the observed performance improvements and guiding future optimization strategies.

In the initial phase of optimizing HSC, doping ZnO (ETL) with 4% Al increased the PCE to 11.39%.

3.2 Effect of AZO thickness

Recent studies have shown that carefully adjusting AZO, especially by improving its transparency, conductivity, and interface characteristics can meaningfully enhance the efficiency and longevity of solar cells [40]. These findings highlight the importance of controlling the properties of AZO films to maximize their performance in solar cells.

A 4% doping level with a ZnO thickness of 0.05 µm was found to produce the greatest performance after analyzing the effect of doping ZnO (ETL) in the ZnO/P3HT HSC. In order to determine the ideal thickness for optimizing the HSC performance, the impact of changing the AZO thickness is further examined in this work utilizing SCAPS software [41]. Plotting the resultant curve in Fig. 7 shows how the AZO thickness and two crucial solar cell parameters V_{OC} and J_{SC} relate to one another. When the AZO layer becomes thicker (from 0.001 µm to 0.05 µm), V_{OC} and J_{SC} steadily decrease, with a more rapid decline observed up

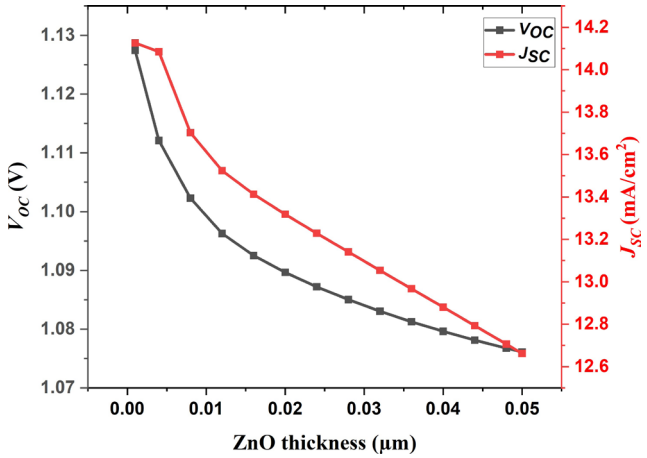

Fig. 7 Impact of ETL thickness on J_{SC} and V_{OC}

to approximately 0.01 µm, followed by a more gradual reduction. By the time the AZO thickness reaches 0.05 µm, V_{OC} has dropped to about 1.075 V. This decline in V_{OC} with increasing AZO thickness can be explained by several factors: increased series resistance, changes in the energy-level alignment at the AZO/active layer interface, and a possible increase in recombination sites within the thicker layer.

For J_{SC}, the reduction is initially more rapid and then more gradual. At an AZO thickness of 0.05 µm, J_{SC} has decreased to about 12.65 mA/cm^2. The decline in J_{SC} can be ascribed to the increased optical absorption by the AZO layer, which diminishes the amount of light reaching the active layer and rises the series resistance, leading to a reduced charge collection efficiency [42, 43].

Because of greater photon loss, a thicker ETL results in lower performance. The ETL absorbs more photons than it transmits to the absorber layer as the AZO layer thickness increases.

As portrayed in Fig. 8, the FF begins at around 76% and increases rapidly up to a thickness of 0.01 µm, eventually

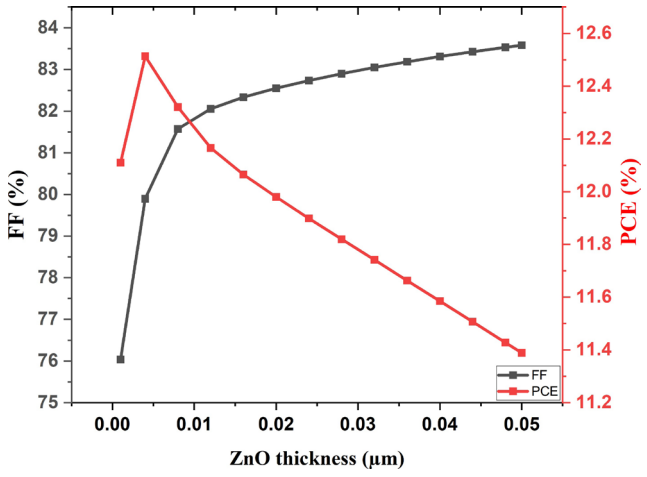

Fig. 8 Effect of ETL thickness on FF and PCE curves

reaching approximately 83.58% at 0.05 µm. After a particular thickness (0.045 µm), the FF tends to level off or decrease; at lesser thicknesses, effective charge extraction takes place, leading to a higher FF [44, 45].

On the other hand, the PCE starts at around 12.1%, peaks at approximately 12.51% with a very thin AZO layer of 0.004 µm, and then gradually declines as the AZO thickness increases, reaching about 11.39% at 0.05 µm.

An AZO thickness of 0.004 µm provides the optimal performance for HSC. This enhancement may be attributed to increased transparency and the occurrence of parasitic ohmic losses with reduced AZO thickness [42, 46]. However, a thickness of 0.004 µm is considered unsuitable for device assembly due to the tripling of surface roughness and the potential for reduced light transparency [47, 48].

The findings on the impact of ETL thickness on solar cell performance are consistent with those reported earlier [44, 45]. For example, we observed a PCE of 12.1% at 0.001 µm AZO thickness, peaking at 12.51% at 0.004 µm and decreasing to 11.39% at 0.05 µm. This trend of initial increase and then decrease in PCE with increasing ETL thickness is also reported [44] where PCE increased from 10% at 0.01 µm to 12% at 0.04 µm and then decreased to 11% at 0.1 µm. Despite the differences in specific device structures, both studies demonstrated similar patterns in how the ETL thickness influences key solar cell parameters.

To elucidate the underlying mechanisms behind the superior efficiency of a thin AZO layer and quantify its impact on charge transport phenomena, a comparative analysis of the recombination current (J_{Rec}) versus bias voltage is conducted for two distinct thicknesses: 0.004 µm (optimal thickness) and 0.05 µm as drawn in Fig. 9.

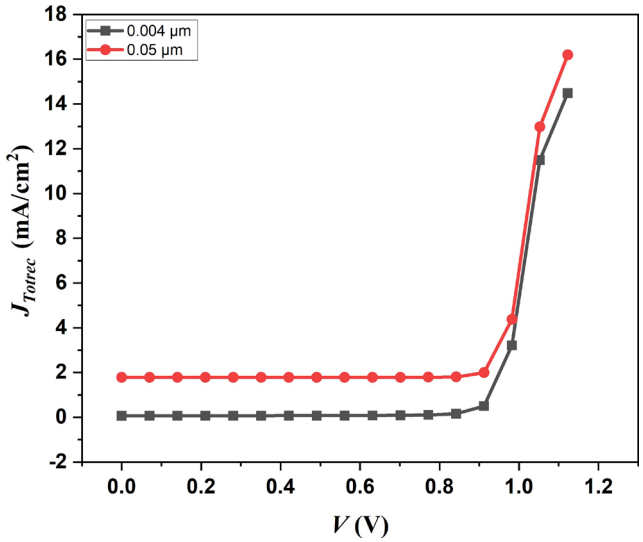

Fig. 9 Effect of ETL thickness (0.004 and 0.05 mm) on the recombination current density versus voltage

This study reveals significant disparities in the recombination characteristics of these devices. The 0.004 µm AZO layer exhibits a negligible recombination current over a wide voltage range (0 to 0.9 V), indicating optimized exciton dissociation, improved charge transport, and a substantial reduction in interfacial recombination losses. In contrast, the 0.05 µm layer shows a constant J_{Rec} of approximately 2 mA/cm^2 within the same voltage range, suggesting an increase in recombination site density correlated with greater thickness. Beyond 0.9 V, both configurations exhibit an exponential increase in J_{Rec}, with slightly higher values for the thicker layer at 1.1 V. This effect is explained by the decrease in the energy barriers that promote recombination processes, which are made worse in thicker layers because of the increased likelihood of carrier trapping. To confirm or refine the hypotheses formulated during the analysis of the J–V and recombination curves, we analyzed the Nyquist diagram for different thicknesses of the AZO layer in an HSC, as portrayed in Fig. 10, where the frequency is in the range of 1 kHz to 1 Hz. It is widely recognized that in Nyquist plots, a semicircle at high frequencies indicates the charge transfer process. The charge transfer resistance (R_{ct}) corresponds to the diameter of the semicircle; a smaller diameter signifies a lower charge transfer resistance [49].

Nyquist diagrams demonstrate the imaginary part of the impedance (Z_{IM}) as a function of its real part (Z_{RE}) for AZO thicknesses ranging from 0.001–0.050 µm. These curves provide crucial information regarding electrochemical processes and charge transport within the device. The curves for thicknesses from 0.012 µm to 0.050 µm nearly overlapped, forming a large semicircle that extended up to approximately 140 kΩ cm^2 on the Z_{RE} axis. In contrast, the curves for thinner layers (0.001–0.008 µm) displayed distinct behaviors. The curve for 0.004 µm (in red) shows

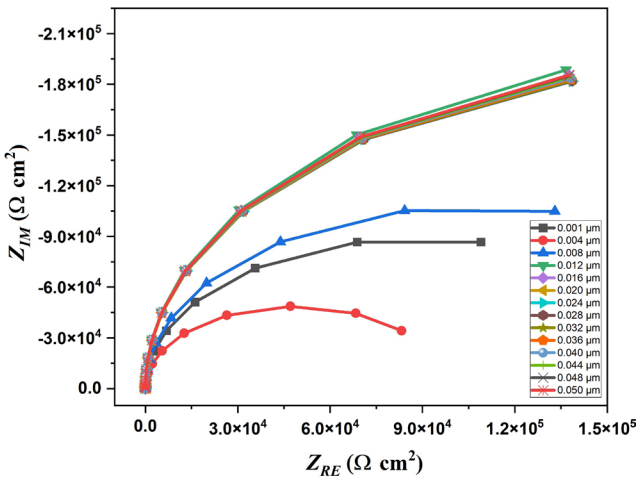

Fig. 10 Nyquist diagrams of HSCs for several AZO thicknesses

a smaller and more defined semicircle, with a maximum Z_{IM} of approximately −50 kΩ cm^2. This shape suggests a reduced charge transfer resistance and potentially better charge separation efficiency at the AZO/active layer interface. A thickness of 0.004 µm appears to offer a good compromise between low charge transfer resistance and sufficient protection of the active layer, corroborating previous results that indicated this thickness is optimal for the overall cell performance. For thicknesses exceeding 0.012 µm, the increase in thickness results in a rise in series resistance and a decrease in light transmission.

By analyzing the Nyquist plots, we determined the R_{ct} values for AZO layers of various thicknesses, as shown in Table 2.

As illustrated in Fig. 10, the arch thickness decreases with a reduction in AZO thickness. Consequently, R_{ct} declines gradually from 140 kΩ cm^2 to 50 kΩ cm^2 as the AZO thickness decreases from 0.05 µm to 0.004 µm, indicating an increase in AZO conductivity with thinner films. Thus, the 0.004 µm thick ZnO layer exhibits the highest conductivity.

To provide additional insights into the dynamics of the electrochemical processes in HSC, we analyzed the curve plotted in Fig. 11, which represents the imaginary part of the impedance (Z_{IM}) as a function of frequency (f) for two AZO thicknesses (0.004 µm and 0.05 µm).

The impedance spectra revealed distinct differences in charge dynamics between the two AZO thicknesses. For both thicknesses, a Z_{IM} peak is observed, with the peak being more pronounced and shifted toward lower frequencies for the 0.05 µm thickness. The maximum amplitude of Z_{IM} for the 0.05 µm layer reaches approximately −190 kΩ cm^2, compared to approximately −50 kΩ cm^2 for the 0.004 µm layer. Additionally, the peak for the 0.004 µm thickness occurs at a higher frequency (approximately 200 Hz) compared to the 0.05 µm thickness (approximately 50 Hz).

The higher amplitude of the Z_{IM} peak for the 0.05 µm thickness indicates a larger interfacial capacitance, suggesting more significant charge accumulation at the AZO/active layer interface. The shift of the peak toward lower frequencies for the 0.05 µm layer implies slower charge transfer processes, corroborating the increased charge transfer resistance observed in the Nyquist plot.

Conversely, the narrower and lower amplitude peak for the 0.004 µm thickness indicates enhanced charge transfer efficiency and less occurrence of recombination phenomena, consistent with the superior overall performance observed for this thickness. The higher frequency of the peak for the 0.004 µm layer indicates faster charge transfer processes, which may explain the improvements in FF and J_{SC} observed in previous analyses.

These findings justify the optimization of the AZO thickness to 0.004 µm, demonstrating better charge transfer dynamics and reduced charge accumulation at the interface, thereby contributing to the overall enhancement of solar cell performance.

3.3 Fabrication challenges and practical implementation

Precision in doping and layer thickness: achieving 4% Al doping in ZnO and ultrathin AZO layers (0.004 µm) requires advanced techniques such as atomic layer deposition (ALD) or magnetron sputtering. While these methods offer high control, they may increase production costs and complexity compared to conventional sol-gel or spray pyrolysis techniques.

3.4 Effect of electron affinity of ETL layer on the performance of the HSC

The electron affinity of the ETL plays a crucial role in determining the alignment of the energy levels between the light-absorbing material and the ETL. This alignment is key to solar cell performance because it shapes the interfaces where the charge carriers move. By influencing these interfaces, the electron affinity of the ETL can have a substantial impact on the overall efficiency of photovoltaic devices [13, 50–54].

Band alignment at the absorber-ETL interface plays a crucial role in charge carrier transport and extraction. Two primary configurations arise: the "cliff" alignment, where the ETL's electron affinity exceeds that of the absorber, facilitating unimpeded electron flow; and the "spike" alignment, which is characterized by a higher absorber conduction band, potentially impeding electron transfer [55, 56].

Therefore, we examined the effect of the varied affinity of the ETL (3.5–4.5 eV) on the performance of the HSC.

Table 2 Charge transfer resistance (R_{ct}) of each AZO layer

AZO thickness (µm)	0.001	0.004	0.008	0.05
Charge transfer resistance (Ω cm^2)	9.0E4	5.0E4	1.1E5	1.4E5

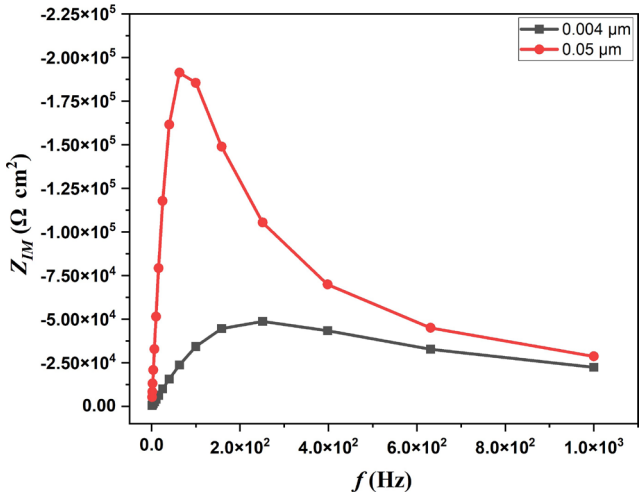

Fig. 11 Imaginary impedance vs. frequency for 0.004 µm and 0.05 µm thickness of AZO

The values of J_{SC}, V_{OC}, FF, and efficiency of the solar cell are recorded and plotted in Figs. 12 and 13, respectively.

As illustrated in Figs. 12 and 13, V_{OC} is positively correlated with the ETL electron affinity. Similarly, the FF and PCE show enhancement as the ETL electron affinity increases from 3.5 to 4.25 eV, which is potentially attributable to the improved electron transport from the absorber to the ETL. However, a decline in FF and PCE is noted when the ETL electron affinity exceeds 4.25 eV, possibly owing to the energetic misalignment between the absorber and ETL interfaces.

As the ETL electron affinity increased, J_{SC} showed a non-monotonic trend. As the electron affinity rises from 3.4 to 4 eV, J_{SC} first is lowering from 14.110 mA/cm^2 to 14.084 mA/cm^2.

The correlation between the electron affinity and device performance in this HSCs can be elucidated through a meticulous examination of the band diagrams shown in Fig. 14 and their corresponding performance metrics. This analysis revealed the intricate interplay between electronic structure and charge transport dynamics across various electron affinity regimes.

In the lower electron affinity range (3.5 eV to 3.95 eV), a significant transformation in interfacial energetics is observed. Fig. 14 (a) illustrates a pronounced conduction band "spike" at the absorber-ETL interface at 3.5 eV, presenting a substantial energetic barrier for electron transport. As the electron affinity increases to 3.95 eV as drawn in Fig. 14 (b), this "spike" is markedly attenuated, promoting better conduction band alignment within the ETL and absorber layers. This transition manifests as a substantial

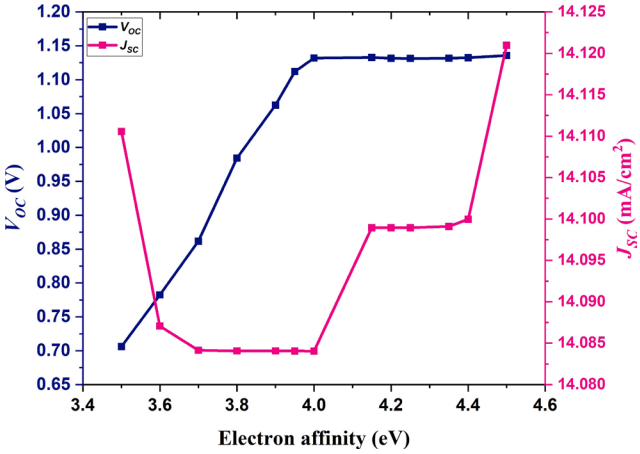

Fig. 12 Effect of ETL electron affinity on V_{OC} and J_{SC} variations

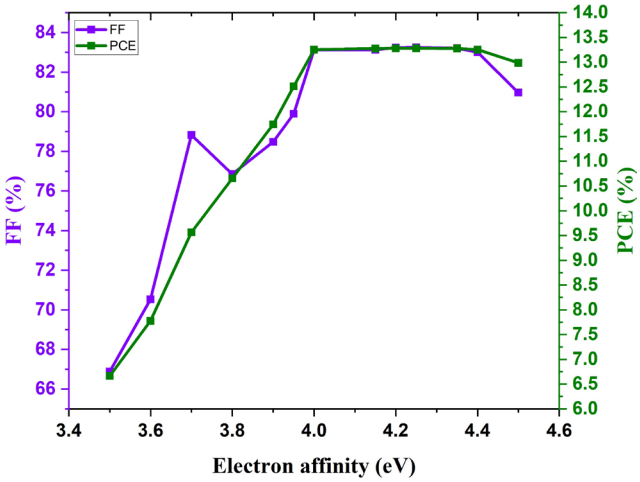

Fig. 13 Effect of ETL electron affinity on FF and PCE variations

enhancement in V_{OC}, and a decrease in J_{SC} is observed, which can be ascribed to the diminished interfacial electric field resulting from the "spike" reduction, temporarily compromising the charge extraction efficiency.

The optimal configuration, which occurs at approximately 4.25 eV, as sketched in Fig. 14 (c), exhibits a near-ideal alignment of the conduction bands at the interface, characterized by the absence of significant energetic barriers for electron transport. This configuration culminates in a maximum V_{OC} and concurrent increase in J_{SC}, which is indicative of optimized charge extraction dynamics.

At higher electron affinities (4.5 eV, Fig. 14 (d)), the emergence of a conduction band "cliff" at the absorber-ETL interface is observed. This feature facilitates the initial electron transfer but potentially introduces energy losses. The continued increase in J_{SC} under these conditions can be ascribed to the enhanced initial electron transfer despite potential compromises in the overall energy conversion efficiency.

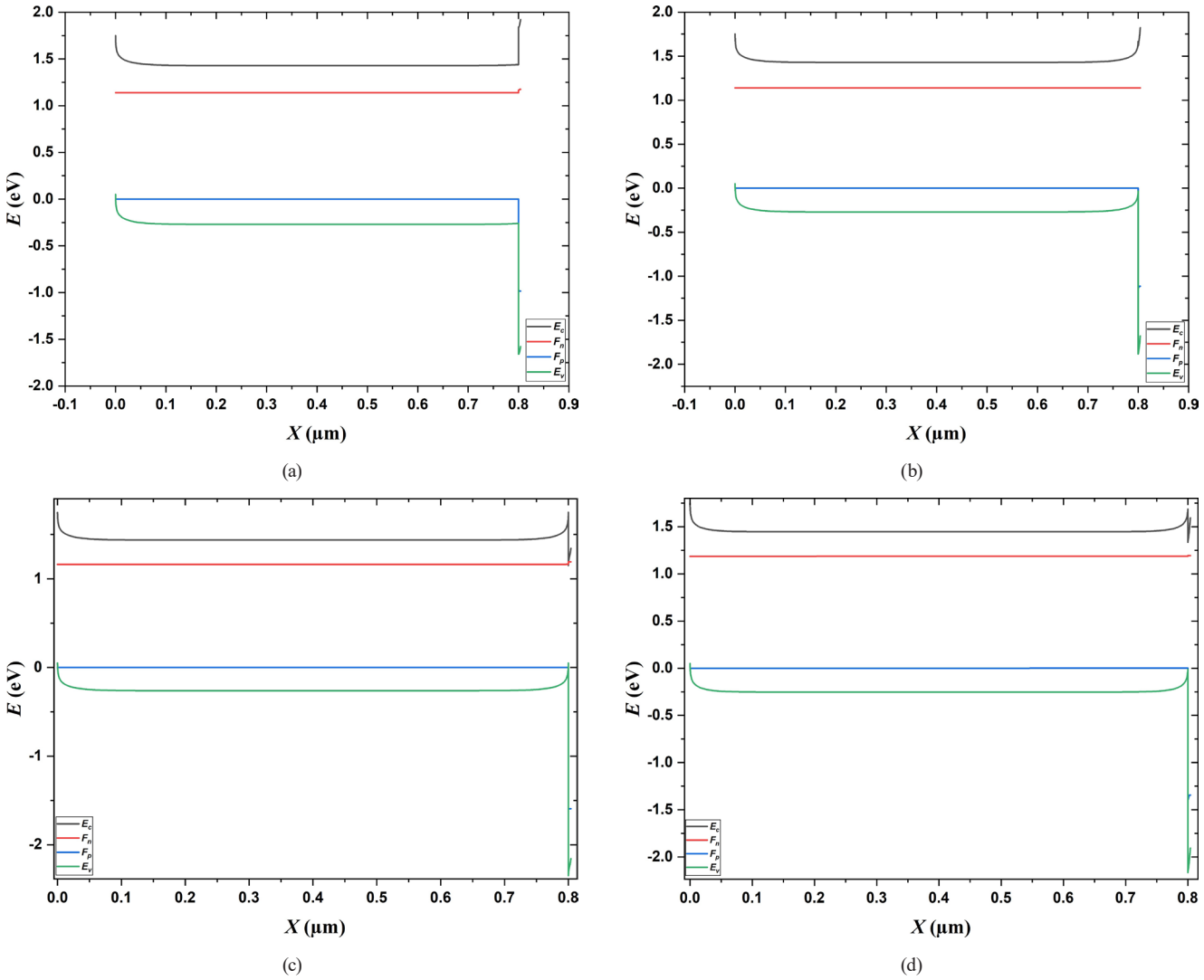

Fig. 14 Band alignment at the AZO/P3HT interface under varying ETL electron affinities: (a) 3.5 eV (spike configuration); (b) 3.95 eV (attenuated spike); (c) 4.25 eV (optimal alignment); (d) 4.5 eV (cliff configuration)

Analysis of the FF and PCE curves corroborates these findings, demonstrating a global performance optimum centered around 4.25 eV, followed by a slight decline at 4.5 eV. This trend underscores the delicate balance between interfacial energy alignment and charge transport efficiency for optimal device performance. The findings align with previous reports [57], who observed a PCE peak at 4.25 eV electron affinity in perovskite solar cells reaching 18.2%, The decline in FF beyond 4.25 eV in both studies suggests universal energetic misalignment effects at high electron affinities.

3.5 Effect of absorber layer thickness

Maximizing solar cell efficiency requires optimizing the thickness of the absorber layer. Prior research has shown that important photovoltaic parameters, including as the J_{SC}, V_{OC}, FF, and PCE, are strongly influenced by the active layer's thickness [58–61]. With thicknesses ranging from 0.5 µm to 6 µm, Figs. 15 and 16 show how the absorber layer thickness affects several device parameters.

The thickness of the active layer and the absorber material's absorption coefficient both have a significant impact on J_{SC}. Even when the charge-carrier diffusion length was exceeded, Fig. 15 shows that J_{SC} increased as active layer thickness increased. Thicker active layers have more photogenerated carriers and better light absorption, which can account for this behavior [54, 60]. This steady rise indicates that under this regime, the charge-carrier generation rate was higher than the recombination rate. On the other hand, when the thickness of the active layer increases, V_{OC} shows a declining tendency. This is because bigger active layers increase the series resistance [62]. As can

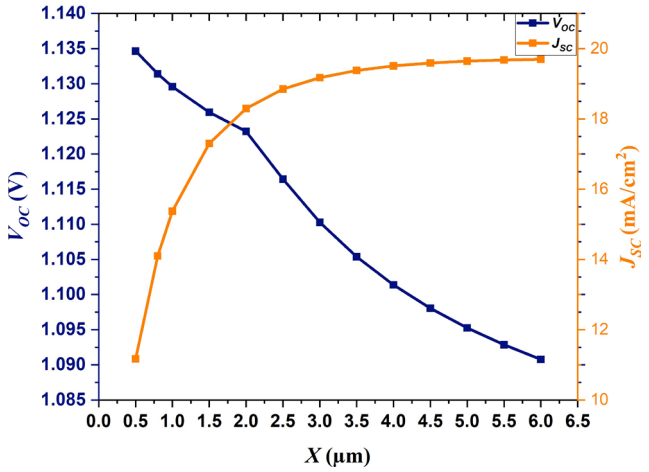

Fig. 15 The thickness of the absorber layer impact on J_{SC} and V_{OC} characteristics

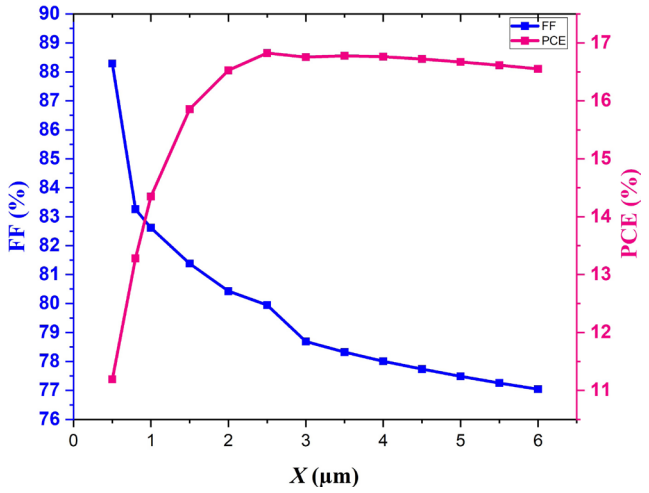

Fig. 16 Absorber film thickness impact on FF and PCE characteristics

be seen in Fig. 16, the PCE first rose as the active layer thickness grew, peaking at 2.5 µm. The active material's high absorption coefficient is responsible for this improvement [56, 63, 64].

Because the charged particles are unable to efficiently pass through the entire thickness to reach the electrodes, the PCE gradually drops beyond this ideal thickness.

Consequently, these charged particles' carrier lifetime ends before they can finish their journey, causing recombination and a reduction in the photovoltaic solar cell's (PSC) performance [65].

Fig. 16 illustrates how the FF also drops as active layer thickness increases. This is mostly because thicker active layers have higher series resistance [54, 66–68]. The maximum PCE in this simulation investigation, at the ideal active-layer thickness of 2.5 µm, is 16.82%. This result emphasizes how crucial it is to precisely adjust the thickness of the absorber layer in high-performance solar cells in order to balance light absorption and charge transfer efficiency.

3.6 Impact of AZO/P3HT interface defect density on electrical parameters of solar cells

Fig. 17 demonstrates that V_{OC} is particularly sensitive to increases in interface defect density. Up to a density of approximately 10^{12} 1/cm^2, V_{OC} remained relatively stable. However, a significant decrease was observed once the density reached 10^{13} 1/cm^2, and this reduction became more pronounced thereafter. Beyond 10^{14} 1/cm^2, V_{OC} experienced a sharp decline. In contrast, the short-circuit current density (J_{SC}) remained remarkably stable, showing almost no change up to 10^{14} 1/cm^2, with only a slight decrease at 10^{15} 1/cm^2, followed by a rapid decline at 10^{16} 1/cm^2. This decline is explained by the higher defect density, which accelerates the rate of carrier recombination at the interface and causes a rapid decrease in J_{SC} [31, 69]. The rapid drop in V_{OC} is also a result of this increase in the rate of carrier recombination at the contact [31, 70].

Fig. 18 illustrates the effect of the defect density at the interface between the ETL (ZnO) and absorber (P3HT) on the FF and PCE of the HSC. Initially, the PCE remained stable at approximately 16.82% for defect densities up to 10^{11} 1/cm^2. However, a gradual decline occurred between 10^{12} and 10^{13} 1/cm^2, followed by a sharp drop after 10^{13} 1/cm^2, reaching approximately 9.5% at 10^{16} 1/cm^2. Similarly, the FF is stable, maintaining approximately 80% up to 10^{13} 1/cm^2. Due to the higher heterojunction resistance of the solar cell brought on by the higher defect density at the main junction interface, there is a sharp decline between 10^{13} and 10^{14} 1/cm^2, with a minimum of roughly 65% [31, 70]. reached around 84% at 10^{16} 1/cm^2 at very high defect density. For additional simulation, the defect density at the AZO/P3HT contact is set to 10^{10} 1/cm^2. A PCE of 18% is obtained for AZO/ZnO-i/CdS/CSTS HSC by integrating an ultra-thin P3HT layer as it is reported [71].

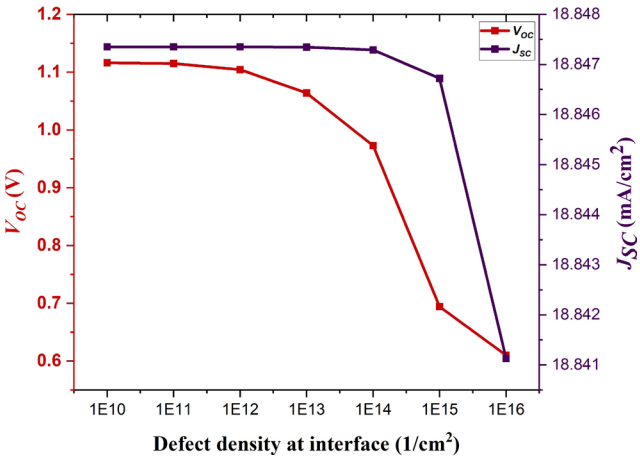

Fig. 17 Effect of interface defect density (ETL/absorber) on a HSC J_{SC} and V_{OC}

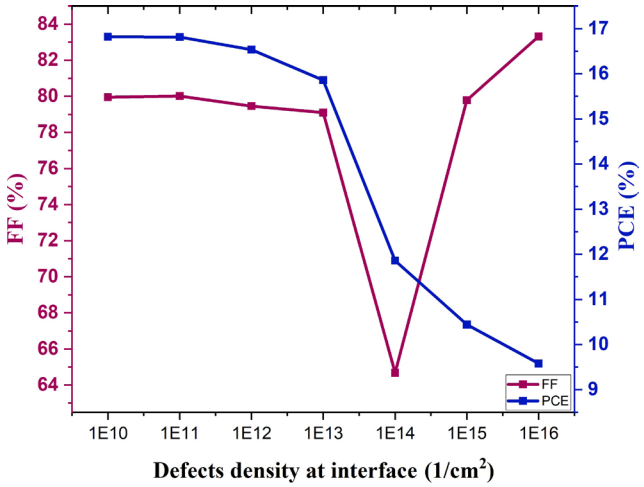

Fig. 18 Impact of interface defect density (ETL/absorber) on the FF and PCE of a HSC

The interface defect density results for ZnO/P3HT correlate with Siddique et al. [45], who reported a critical threshold of 10^{13} 1/cm^2 for indium–gallium–zinc oxide (IGZO)/Sb_2S_3 interfaces (PCE drop from 14.2% to 9.1% and the PCE of our structure drop from 16.82% to 9.5%). The higher baseline PCE in the work underscores P3HT's superior defect tolerance compared to Sb_2S_3. Both studies revealed a consistent pattern in the behavior of key performance parameters as a function of the interface defect density.

Maintaining interface defect densities below 10^{13} 1/cm^2 necessitates stringent fabrication conditions like cleanroom environments and post-deposition treatments as annealing and plasma passivation. Industrial scalability of such defect mitigation strategies remains a challenge.

3.7 Impact of operating temperature

Temperature significantly affects several physical parameters, including charge diffusion, carrier mobility, resistance, band gap, and specific heat [63]. Consequently, it is essential to conduct a comprehensive analysis of how temperature influences device performance.

This study examined the temperature-dependent performance of an AZO/P3HT HSC over a temperature range of 273–348 K. As the functional temperature of the cell increased, we observed a complex interplay between the thermal effects and the charge carrier behavior. Initially, the temperature increase provided electrons with additional thermal energy, potentially enhancing charge generation and transport processes. However, thermal activation is not uniformly beneficial. At higher temperatures, we note an increased likelihood of electron-hole recombination before the carriers can effectively reach the depletion region. This phenomenon suggests that while moderate temperature increases may improve cell functionality, excessive thermal energy can ultimately degrade performance by promoting premature charge recombination. The findings underscore the critical importance of thermal management in optimizing the efficiency of hybrid organic-inorganic photovoltaic devices [64].

Fig. 19 depicts the temperature-dependent behavior of V_{OC} and J_{SC} in the AZO/P3HT HSC over the range 273–348 K. A near-linear decline in V_{OC} is observed, decreasing from approximately 1.16 V at 273 K to 1.01 V at 348 K. This reduction in V_{OC} with increasing temperature is a characteristic phenomenon in solar cells, and is attributed to the formation of additional interfacial defects, increased series resistance, and diminished carrier diffusion length [72, 73].

Conversely, J_{SC} exhibits a temperature-induced increase from 18.77 mA/cm^2 at 273 K to 18.90 mA/cm^2 at 348 K. The growth rate is more pronounced at lower temperatures, before plateauing at higher temperatures. This J_{SC} enhancement is primarily due to the narrowing of the energy band gap and increased electron-hole pair generation at elevated temperatures [72–74].

As illustrated in Fig. 20, the FF demonstrated an overall upward trend with temperature, initiating at approximately 75% at 273 K and reaching approximately 86% at 348 K. This improvement in the FF can be ascribed to the enhanced charge carrier mobility and reduced series resistance at higher temperatures.

The PCE exhibits a more complex temperature dependence. It increases from 273 K to 313 K, peaking at 17.13%. A sharp decline is observed between 313 K and 320 K,

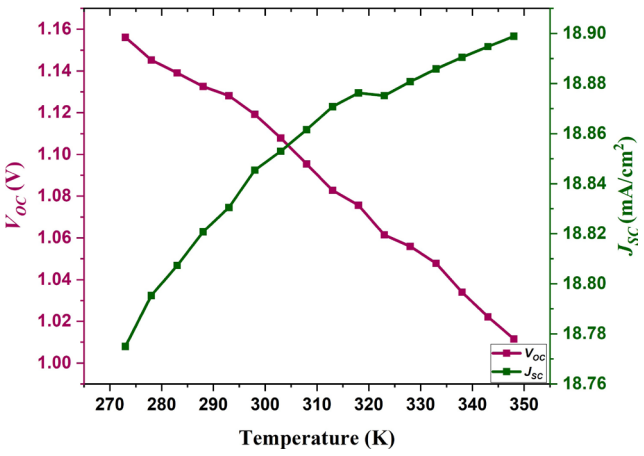

Fig. 19 Impact of operating temperature on V_{OC} and J_{SC} curves

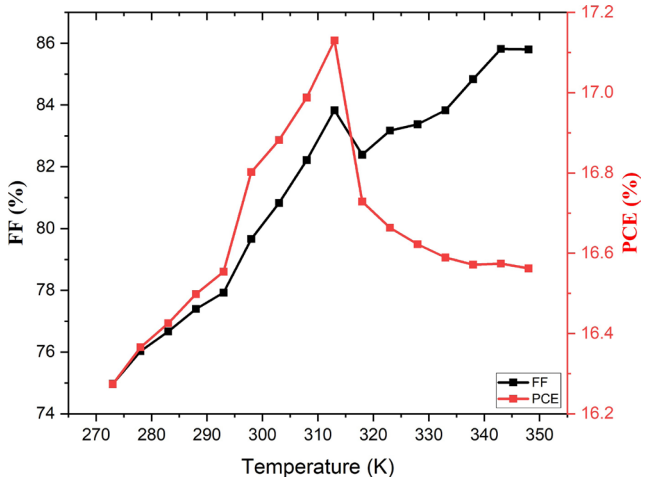

Fig. 20 Impact of operating temperature on FF and PCE curves

followed by a gradual decrease, stabilizing at approximately 16.6% at higher temperatures. The initial PCE increase (273–313 K) likely stems from improved charge generation and transport. The 313 K peak represents the optimal operating temperature, balancing the benefits of increased charge mobility and J_{SC} against the drawbacks of increased recombination and a lower V_{OC}.

Beyond this optimal point, the solar cell efficiency decreased as the temperature increased further. This decline is attributed to temperature-induced changes in the material carrier concentration, band gaps, and charge carrier mobility [73]. The temperature-dependent analysis agrees with previous work [72], which recorded a 1.5% PCE drop in $CH_3NH_3PbI_3$ ($MAPbI_3$) solar cells between 300–320 K, compared to our 0.53% decline (313–320 K). The solar cell demonstrates superior performance at lower temperatures, with a noticeable degradation as the temperature increases [57–59].

3.8 Comparison of the findings with literature on the effect of doping ZnO with various dopants in different solar sell structures

Table 3 shows ZnO as the ETL, the different dopants, year, and PCE values of our work compared to those previously reported [10, 11, 60–62, 65–71, 75–79].

Table 3 ZnO as an ETL, different dopants, year, and PCE values of our work/others works and references

Solar cell	ETL	Dopant	Year	PCE (%) after doping	Reference
HSC	ZnO	Al	2024	17.13	Our simulation results by Scaps
PSC	ZnO	Al	2023	7	[10]
Planar PSC	ZnO	Graphene oxide silver-doped bilayer, reduced graphene oxide/Ag-doped	2021	11.03	[11]
PSC	ZnO	Al	2016	12.6	[75]
Heterojunction solar cell	ZnO	Al	2022	8.984	[60]
Pbs quantum dots solar cell	ZnO	Mg	2021	9.46	[60]
Inverted polymer solar cell	ZnO	In	2021	5.99	[61]
Flexible PSC	ZnO	Co	2020	7	[62]
Polymer solar cell	ZnO	Au	2020	8.801	[65]
Dye-sensitized solar cell (DSSC)	ZnO	Mn	2020	4.20	[66]
Inverted polymer solar cell	ZnO	Ga	2019	7.7	[67]
Organic solar cell	ZnO	Li, Ce, Li/Ce	2019	9.074	[68]
PSC	ZnO	Al	2019	7	[69]
Organic solar cell	ZnO	Al	2019	3.24	[70]
Inverted polymer solar cell	ZnO	Al	2016	3.25	[76]
$Pt/CuSbS_2/CH_3NH_3PbI_3/HC(NH_2)_2PbI_3/ZnO/FTO$ PSC	ZnO	–	2023	38.53	[77]
$FTO/ZnO/MASnI_3/CsSnC_{l3}/NiO/Pt$ PSC	ZnO	–	2024	31.45	[78]
$Au/MoO_3/Cs_2TiBr_6/MASnBr_3/ZnO/FTO$ PSC	ZnO	–	2024	32.96	[79]
AZO/ZnO-exolain i/CdS/CSTS	ZnO	–	2024	18.24	[71]

4 Conclusion

Through a comprehensive investigation of the critical parameters, this study offers important insights into the optimization of Cu/ZnO/P3HT/Pt HSCs. Aluminum doping of ZnO to 4% and adjusting the AZO thickness to 4 nm significantly improved the PCE from 9.9% to 12.51%. Further optimization of the electron affinity (4.25 eV) and absorber layer thickness (2.5 μm) pushed the PCE to 16.82%.

The results indicate stable device performance at interface defect densities below 10^{13} 1/cm^2, with degradation occurring beyond this threshold. The temperature analysis identified 313 K as the optimal operating condition, yielding a peak PCE of 17.13%.

The simulations achieved a 17.13% PCE, surpassing prior Al-doped ZnO-based HSCs as 12.6% in earlier papers as reported by Zhao et al. [7] and 9.46% by Xing et al. [60], respectively.

These results enhance the understanding of HSC performance and provide a foundation for future research and practical applications. This study explanation of the intricate interactions between several device characteristics provides a road map for creating next-generation photovoltaics with high efficiency, which could hasten the shift to sustainable energy sources.

Acknowledgment

The work is included in the PRFU project under contract number B00L02UN310220220001 Oran University of Sciences and Technology USTO-MB.

A big thank you to any student who followed my advice and believed in my advice. In our FDFCA RG "work hard and work fast" InshAllah you succeed.

References

[1] Correa-Baena, J.-P., Saliba, M., Buonassisi, T., Grätzel, M., Abate, A., Tress, W., Hagfeldt, A. "Promises and challenges of perovskite solar cells", Science, 358(6364), pp. 739–744, 2017. https://doi.org/10.1126/science.aam6323

[2] Yu, X., Yu, X., Yan, M., Weng, T., Chen, L., Zhou, Y., Wei, J. "Lowering oxygen vacancies of ZnO nanorods via Mg-doping and their effect on polymeric diode behavior", Sensors and Actuators A: Physical, 312, 112163, 2020. https://doi.org/10.1016/j.sna.2020.112163

[3] Weng, T., Yan, M., Yu, X., Qiao, Q., Zhou, Y., Li, Z., Wei, J., Yu, X. "Light scattering enhancement of ZnO nanorods via Mg–Al co-doping and their influence on polymeric photodetector", Optical Materials, 121, 111516, 2021. https://doi.org/10.1016/j.optmat.2021.111516

[4] Beek, W. J. E., Wienk, M. M., Janssen, R. A. J. "Hybrid Solar Cells from Regioregular Polythiophene and ZnO Nanoparticles", Advanced Functional Materials, 16(8), pp. 1112–1116, 2006. https://doi.org/10.1002/adfm.200500573

[5] Sekine, N., Chou, C.-H., Kwan, W. L., Yang, Y. "ZnO nanoridge structure and its application in inverted polymer solar cell", Organic Electronics, 10(8), pp. 1473–1477, 2009. https://doi.org/10.1016/j.orgel.2009.08.011

[6] Olson, D. C., Shaheen, S. E., Collins, R. T., Ginley, D. S. "The Effect of Atmosphere and ZnO Morphology on the Performance of Hybrid Poly(3-hexylthiophene)/ZnO Nanofiber Photovoltaic Devices", The Journal of Physical Chemistry C, 111(44), pp. 16670–16678, 2007. https://doi.org/10.1021/jp0734225

[7] Zhao, X., Shen, H., Zhang, Y., Li, X., Zhao, X., Tai, M., Li, J., Li, J., Li, X., Lin, H. "Aluminum-Doped Zinc Oxide as Highly Stable Electron Collection Layer for Perovskite Solar Cells", ACS Applied Materials & Interfaces, 8(12), pp. 7826–7833, 2016. https://doi.org/10.1021/acsami.6b00520

[8] Gahtar, A., Rahal, A., Benhaoua, B., Benramache, S. "A comparative study on structural and optical properties of ZnO and Al-doped ZnO thin films obtained by ultrasonic spray method using different solvents", Optik, 125(14), pp. 3674–3678, 2014. https://doi.org/10.1016/j.ijleo.2014.01.078

[9] Al-Ghamdi, A. A., Al-Hartomy, O. A., El Okr, M., Nawar, A. M., El-Gazzar, S., El-Tantawy, F., Yakuphanoglu, F. "Semiconducting properties of Al doped ZnO thin films", Spectrochimica Acta Part A: Molecular and Biomolecular Spectroscopy, 131, pp. 512–517, 2014. https://doi.org/10.1016/j.saa.2014.04.020

[10] Bag, A., Radhakrishnan, R., Nekovei, R., Jeyakumar, R. "Effect of absorber layer, hole transport layer thicknesses, and its doping density on the performance of perovskite solar cells by device simulation", Solar Energy, 196, pp. 177–182, 2020. https://doi.org/10.1016/j.solener.2019.12.014

[11] Zandi, S., Saxena, P., Gorji, N. E. "Numerical simulation of heat distribution in RGO-contacted perovskite solar cells using COMSOL", Solar Energy, 197, pp. 105–110, 2020. https://doi.org/10.1016/j.solener.2019.12.050

[12] Gharibshahian, I., Orouji, A. A., Sharbati, S. "Towards high efficiency Cd-Free Sb_2Se_3 solar cells by the band alignment optimization", Solar Energy Materials and Solar Cells, 212, 110581, 2020. https://doi.org/10.1016/j.solmat.2020.110581

[13] Burgelman, M., Nollet, P., Degrave, S. "Modelling polycrystalline semiconductor solar cells", Thin Solid Films, 361–362, pp. 527–532, 2000. https://doi.org/10.1016/S0040-6090(99)00825-1

[14] Ngue, P. G. D. K., Ngoupo, A. T., Abena, A. M. N., Abega, F. X. A., Ndjaka, J.-M. B. "Investigation of the Performance of a Sb_2S_3-Based Solar Cell with a Hybrid Electron Transport Layer (h-ETL): A Simulation Approach Using SCAPS-1D Software", International Journal of Photoenergy, 2024(1), 5188636, 2024. https://doi.org/10.1155/2024/5188636

[15] Ngoupo, A. T., Ouédraogo, S., Zougmoré, F., Ndjaka, J. M. B. "Numerical analysis of ultrathin Sb_2Se_3-based solar cells by SCAPS-1D numerical simulator device", Chinese Journal of Physics, 70, pp. 1–13, 2021. https://doi.org/10.1016/j.cjph.2020.12.010

[16] Zhao, G., Wang, W., Bae, T.-S., Lee, S.-G., Mun, C., Lee, S., Yu, H., Lee, G.-H., Song, M., Yun, J. "Stable ultrathin partially oxidized copper film electrode for highly efficient flexible solar cells", Nature Communications, 6(1), 8830, 2015. https://doi.org/10.1038/ncomms9830

[17] Liu, Z., Lee, S. Y., Lee, E.-C. "Copper nanoparticle incorporated plasmonic organic bulk-heterojunction solar cells", Applied Physics Letters, 105(22), 223306, 2014. https://doi.org/10.1063/1.4903749

[18] Mittal, V. "Researchers to Lower Solar Cell Costs by Replacing Silver with Copper", Avaada, 01 October 2024. [online] Available at: https://avaada.com/researchers-to-lower-solar-cell-costs-by-replacing-silver-with-copper/ [Accessed: 06 May 2025]

[19] Swami, S. K., Khan, J. I., Dutta, V., Lee, J., Laquai, F., Chaturvedi, N. "Spray-Deposited Aluminum-Doped Zinc Oxide as an Efficient Electron Transport Layer for Inverted Organic Solar Cells", ACS Applied Energy Materials, 6(5), pp. 2906–2913, 2023. https://doi.org/10.1021/acsaem.2c03858

[20] Patel, N. "Characterization of Electrical Performance of Aluminum-Doped Zinc Oxide Pellets", DePaul Discoveries, 3(1), 6, 2014. [online] Available at: https://via.library.depaul.edu/depaul-disc/vol3/iss1/6 [Accessed: 06 May 2025]

[21] Momot, A., Amini, M. N., Reekmans, G., Lamoen, D., Partoens, B., Slocombe, D. R., Elen, K., Adriaensens, P., Hardy, A., Van Bael, M. K. "A novel explanation for the increased conductivity in annealed Al-doped ZnO: an insight into migration of aluminum and displacement of zinc", Physical Chemistry Chemical Physics, 19(40), pp. 27866–27877, 2017. https://doi.org/10.1039/C7CP02936E

[22] Anrango-Camacho, C., Pavón-Ipiales, K., Frontana-Uribe, B. A., Palma-Cando, A. "Recent Advances in Hole-Transporting Layers for Organic Solar Cells", Nanomaterials, 12(3), 443, 2022. https://doi.org/10.3390/nano12030443

[23] Mech, W., Borysiuk, J., Wincukiewicz, A., Bożek, R., Trautman, P., Tokarczyk, M., Kamińska, M., Korona, K. P. "Influence of Active Layer Processing on Electrical Properties and Efficiency of Polymer–Fullerene Organic Solar Cells", Acta Physica Polonica A, 136(4), pp. 579–584, 2019. https://doi.org/10.12693/APhysPolA.136.579

[24] Korte, D., Pavlica, E., Klančar, D., Bratina, G., Pawlak, M., Gondek, E., Song, P., Liu, J., Derkowska-Zielinska, B. "Influence of P3HT:PCBM Ratio on Thermal and Transport Properties of Bulk Heterojunction Solar Cells", Materials, 16(2), 617, 2023. https://doi.org/10.3390/ma16020617

[25] Andreas, T. "P3HT:PCPDTBT:PCBM Multi-polymer single layer solar cells", DigitalCommons@CalPoly, 11 November 2012. [online] Available at: https://digitalcommons.calpoly.edu/cgi/viewcontent.cgi?article=1067&context=physsp [Accessed: 06 May 2025]

[26] Behrouznejad, F., Shahbazi, S., Taghavinia, N., Wu, H.-P., Diau, E. W.-G. "A study on utilizing different metals as the back contact of $CH_3NH_3PbI_3$ perovskite solar cells", Journal of Materials Chemistry A, 4(35), pp. 13488–13498, 2016. https://doi.org/10.1039/C6TA05938D

[27] Zeiske, S., Sandberg, O. J., Zarrabi, N., Li, W., Meredith, P., Armin, A. "Direct observation of trap-assisted recombination in organic photovoltaic devices", Nature Communictaions,12(1), 3603, 2021. https://doi.org/10.1038/s41467-021-23870-x

[28] MacKenzie, R. C. I., Kirchartz, T., Dibb, G. F. A., Nelson, J. "Modeling Nongeminate Recombination in P3HT:PCBM Solar Cells", The Journal of Physical Chemistry C, 115(19), pp. 9806–9813, 2011. https://doi.org/10.1021/jp200234m

[29] Moiz, S. A. "Optimization of Hole and Electron Transport Layer for Highly Efficient Lead-Free Cs_2TiBr_6-Based Perovskite Solar Cell", Photonics, 9(1), 23, 2022. https://doi.org/10.3390/photonics9010023

[30] Bin, H., Yang, Y., Peng, Z., Ye, L., Yao, J., Zhong, L., Sun, C., …, Li, Y. "Effect of Alkylsilyl Side-Chain Structure on Photovoltaic Properties of Conjugated Polymer Donors", Advanced Energy Materials, 8(8), 1702324, 2018. https://doi.org/10.1002/aenm.201702324

[31] Zidan, M. N., Ismail, T., Fahim, I. S. "Effect of thickness and temperature on flexible organic P3HT:PCBM solar cell performance", Materials Research Express, 8(9), 095508, 2021. https://doi.org/10.1088/2053-1591/ac2773

[32] Kumar Das, M., Panda, S., Mohapatra, N. "Power conversion efficiency optimization of $LaFeO_3$ Mott insulator based solar cell with metal oxide transport layers using SCAPS", Materials Today: Proceedings, 74, pp. 756–762, 2023. https://doi.org/10.1016/j.matpr.2022.11.031

[33] Kirchartz, T., Pieters, B. E., Kirkpatrick, J., Rau, U., Nelson, J. "Recombination via tail states in polythiophene:fullerene solar cells", Physical Review B, 83(11), 115209, 2011. https://doi.org/10.1103/PhysRevB.83.115209

[34] Raeyani, D., Asgari, A. "Enhancing the Efficiency of Inverted Organic Solar Cells with Treatment Techniques: Numerical and Experimental Study", International Journal of Energy Research, 2023(1), 6612574, 2023. https://doi.org/10.1155/2023/6612574

[35] Mohd Alias, N. S. N., Arith, F., Mustafa, A. N., Ismail, M. M., Azmi, N. F., Saidon, M. S. "Impact of Al on ZnO Electron Transport Layer in Perovskite Solar Cells", Journal of Engineering and Technological Sciences, 54(4), 220409, 2022. https://doi.org/10.5614/j.eng.technol.sci.2022.54.4.9

[36] Mahmood, K., Park, S. B. "Atmospheric pressure based electrostatic spray deposition of transparent conductive ZnO and Al-doped ZnO (AZO) thin films: Effects of Al doping and annealing treatment", Electronic Materials Letters, 9(2), pp. 161–170, 2013. https://doi.org/10.1007/s13391-012-2188-6

[37] Mugwang'a, F. K., Karimi, P. K., Njoroge, W. K., Omayio, O. "Characterization of Aluminum Doped Zinc Oxide (Azo) Thin Films Prepared by Reactive Thermal Evaporation for Solar Cell Applications", Journal of Fundamentals of Renewable Energy and Applications, 5(4), 1000170, 2015. https://doi.org/10.4172/2090-4541.1000170

[38] Mahmood, K., Swain, B. S., Jung, H. S. "Controlling the surface nanostructure of ZnO and Al-doped ZnO thin films using electrostatic spraying for their application in 12% efficient perovskite solar cells", Nanoscale, 6(15), pp. 9127–9138, 2014. https://doi.org/10.1039/C4NR02065K

[39] Baltakesmez, A., Biber, M., Tüzemen, S. "Inverted planar perovskite solar cells based on Al doped ZnO substrate!, Journal of Radiation Research and Applied Sciences, 11(2), pp. 124–129, 2018. https://doi.org/10.1016/j.jrras.2017.11.002

[40] Kruszyńska, J., Ostapko, J., Ozkaya, V., Surucu, B., Szawcow, O., Nikiforow, K., Hołdyński, M., …, Prochowicz, D. "Atomic Layer Engineering of Aluminum-Doped Zinc Oxide Films for Efficient and Stable Perovskite Solar Cells", Advanced Materials Interfaces, 9(17), 2200575, 2022. https://doi.org/10.1002/admi.202200575

[41] University of Gent, Department of Electronics and Information Systems (ELIS) "SCAPS software, (3.3.2.0)", [computer program] Available at: http://scaps.elis.ugent.be/ [Accessed: 04 October 2021]

[42] Gogoi, D., Bhattarai, S., Das, T. D. "A numerical investigation for performance enhancement of organic solar cell using Al-doped zinc oxide anode", Indian Journal of Physics, 98(8), pp. 2705–2717, 2024. https://doi.org/10.1007/s12648-023-03042-x

[43] Bhattarai, S., Pandey, R., Madan, J., Muchahary, D., Gogoi, D. "A novel graded approach for improving the efficiency of lead-free perovskite solar cells", Solar Energy, 244, pp. 255–263, 2022. https://doi.org/10.1016/j.solener.2022.08.030

[44] Benali, H., Hartiti, B., Lmai, F., Batan, A., Fadili, S., Thevenin, P. "Enhancing the efficiency of the organic-inorganic hybrid perovskite cells using Al-doped ZnO as an Electron Transport Layer and CNTs as a Hole Transport Layer: An experimental and numerical study", Optik, 304, 171733, 2024. https://doi.org/10.1016/j.ijleo.2024.171733

[45] Siddique, A., Nurul Islam, M., Karmaker, H., Asif Iqbal, A. K. M., Al Mazed Khan, A., Aminul Islam, M., Kumar Das, B. "Numerical modelling and performance investigation of inorganic Copper-Tin-Sulfide (CTS) based perovskite solar cell with SCAPS-1D", Results in Optics, 16, 100713, 2024. https://doi.org/10.1016/j.rio.2024.100713

[46] Chandra, W., Ang, L. K., Pey, K. L., Ng, C. M. "Two-dimensional analytical Mott-Gurney law for a trap-filled solid", Applied Physics Letters, 90(15), 153505, 2007. https://doi.org/10.1063/1.2721382

[47] Gogoi, D., Das, T. D. "The role of a highly optimized approach with superior transparent conductive oxide anode towards efficient organic solar cell", Physica Scripta, 98(8), 085908, 2023. https://doi.org/10.1088/1402-4896/ace1b5

[48] Schafferhans, J., Baumann, A., Wagenpfahl, A., Deibel, C., Dyakonov, V. "Oxygen doping of P3HT:PCBM blends: Influence on trap states, charge carrier mobility and solar cell performance", Organic Electronics, 11(10), pp. 1693–1700, 2010. https://doi.org/10.1016/j.orgel.2010.07.016

[49] Ozel, K., Yildiz, A. "High-performance transparent AZO UV photodetectors", Optical and Quantum Electronics, 56(7), 1258, 2024. https://doi.org/10.1007/s11082-024-07169-x

[50] Hima, A., Lakhdar, N., Benhaoua, B., Saadoune, A., Kemerchou, I., Rogti, F. "An optimized perovskite solar cell designs for high conversion efficiency", Superlattices and Microstructures, 129, pp. 240–246, 2019. https://doi.org/10.1016/j.spmi.2019.04.007

[51] Stolterfoht, M., Caprioglio, P., Wolff, C. M., Márquez, J. A., Nordmann, J., Zhang, S., Rothhardt, D., …, Neher, D. "The impact of energy alignment and interfacial recombination on the internal and external open-circuit voltage of perovskite solar cells", Energy & Environmental Science, 12(9), pp. 2778–2788, 2019. https://doi.org/10.1039/C9EE02020A

[52] Wang, Q., Mosconi, E., Wolff, C., Li, J., Neher, D., De Angelis, F., Suranna, G. P., Grisorio, R., Abate, A. "Rationalizing the Molecular Design of Hole-Selective Contacts to Improve Charge Extraction in Perovskite Solar Cells", Advanced Energy Materials, 9(28), 1900990, 2019. https://doi.org/10.1002/aenm.201900990

[53] Rai, S., Pandey, B. K., Dwivedi, D. K. "Modeling of highly efficient and low cost $CH_3NH_3Pb(I_{1-x}Cl_x)_3$ based perovskite solar cell by numerical simulation", Optical Materials, 100, 109631, 2020. https://doi.org/10.1016/j.optmat.2019.109631

[54] Chen, Q., Ni, Y., Dou, X., Yoshinori, Y. "The Effect of Energy Level of Transport Layer on the Performance of Ambient Air Prepared Perovskite Solar Cell: A SCAPS-1D Simulation Study", Crystals, 12(1), 68, 2022. https://doi.org/10.3390/cryst12010068

[55] Minemoto, T., Murata, M. "Theoretical analysis on effect of band offsets in perovskite solar cells", Solar Energy Materials and Solar Cells, 133, pp. 8–14, 2015. https://doi.org/10.1016/j.solmat.2014.10.036

[56] Nikfar, N., Memarian, N. "Theoretical study on the effect of electron transport layer parameters on the functionality of double-cation perovskite solar cells", Optik, 258, 168932, 2022. https://doi.org/10.1016/j.ijleo.2022.168932

[57] Rai, N., Rai, S., Singh, P. K., Lohia, P., Dwivedi, D. K. "Analysis of various ETL materials for an efficient perovskite solar cell by numerical simulation", Journal of Materials Science: Materials in Electronics, 31(19), pp. 16269–16280, 2020. https://doi.org/10.1007/s10854-020-04175-z

[58] Smith, A. M., Nie, S. "Semiconductor Nanocrystals: Structure, Properties, and Band Gap Engineering", Accounts of Chemical Research, 43(2), pp. 190–200, 2010. https://doi.org/10.1021/ar9001069

[59] Naureen, Sadanand, Lohia, P., Dwivedi, D. K., Ameen, S. "A Comparative Study of Quantum Dot Solar Cell with Two Different ETLs of WS_2 and IGZO Using SCAPS-1D Simulator", Solar, 2(3), pp. 341–353, 2022. https://doi.org/10.3390/solar2030020

[60] Xing, M., Wei, Y., Wang, D., Shen, Q., Wang, R. "Mg-doped ZnO layer to enhance electron transporting for PbS quantum dot solar cells", Current Applied Physics, 21, pp. 14–19, 2021. https://doi.org/10.1016/j.cap.2020.09.014

[61] Luo, J., Feng, Z., Liu, X., Li, Z. "Improved Photovoltaic Characteristics of Inverted Polymer Solar Cells With Indium-Doped ZnO at Low-Temperature Annealing as Electron-Transport Layer", IEEE Journal of Photovoltaics,11(2), pp. 374–378, 2021. https://doi.org/10.1109/JPHOTOV.2021.3051157

[62] Bouhjar, F., Derbali, L., Marí, B. "High performance novel flexible perovskite solar cell based on a low-cost-processed ZnO:Co electron transport layer", Nano Research, 13(9), pp. 2546–2555, 2020. https://doi.org/10.1007/s12274-020-2896-4

[63] Piñón Reyes, A. C., Ambrosio Lázaro, R. C., Monfil Leyva, K., Luna López, J. A., Flores Méndez, J., Heredia Jiménez, A. H., Muñoz Zurita, A. L., Severiano Carrillo, F., Ojeda Durán, E. "Study of a Lead-Free Perovskite Solar Cell Using CZTS as HTL to Achieve a 20% PCE by SCAPS-1D Simulation", Micromachines, 12(12), 1508, 2021. https://doi.org/10.3390/mi12121508

[64] Amiri, I. S., Ahmad, H., Ariannejad, M. M., Ismail, M. F., Thambiratnam, K., Yasin, M., Nik Abdul-Aziz, N. M. A. "Performance Analysis of Copper Tin Sulfide, Cu_2SnS_3 (CTS) with Various Buffer Layers by Using SCAPS in Solar Cells", Surface Review and Letters, 24(06), 1750073, 2017. https://doi.org/10.1142/S0218625X17500731

[65] Sun, Y., Ren, G., Han, S., Zhang, X., Liu, C., Li, Z., Fu, D., Guo, W. "Improving light harvesting and charge extraction of polymer solar cells upon buffer layer doping", Solar Energy, 202, pp. 80–85, 2020. https://doi.org/10.1016/j.solener.2020.03.105

[66] Akman, E. "Enhanced photovoltaic performance and stability of dye-sensitized solar cells by utilizing manganese-doped ZnO photoanode with europium compact layer", Journal of Molecular Liquids, 317, 114223, 2020. https://doi.org/10.1016/j.molliq.2020.114223

[67] Diana, R., Panunzi, B., Morvillo, P., Bobeico, E., Caruso, U. "A Comparative Study on Low-Temperature Sol-Gel Ga-Doped Zinc Oxide Inverted PSCs", International Journal of Electrochemical Science, 14(11), pp. 10281–10288, 2019. https://doi.org/10.20964/2019.11.13

[68] Wang, M., Sun, Y., Guo, J., Li, Z., Liu, C., Guo, W. "Alkali metal salts doped ZnO interfacial layers facilitate charge transport for organic solar cells", Organic Electronics, 74, pp. 258–264, 2019. https://doi.org/10.1016/j.orgel.2019.07.020

[69] Spalla, M., Planes, E., Perrin, L., Matheron, M., Berson, S., Flandin, L. "Alternative Electron Transport Layer Based on Al-Doped ZnO and SnO_2 for Perovskite Solar Cells: Impact on Microstructure and Stability", ACS Applied Energy Materials, 2(10), pp. 7183–7195, 2019. https://doi.org/10.1021/acsaem.9b01160

[70] Kadem, B. Y., Mohammed Ali, M. J., Abdulameer, A. F. "The Effects of Al-Doped ZnO Layer on the Performance of Organic Solar Cell", In: 2019 12th International Conference on Developments in eSystems Engineering (DeSE), Kazan, Russia, 2019, pp. 741–746. ISBN 978-1-7281-3022-4 https://doi.org/10.1109/DeSE.2019.00138

[71] Merzougui, L., Benhaliliba, M., Ayeshamariam, A. "Enhancing the performance of AZO/ZnO-i/CdS/ CSTS hybrid solar cell by incorporating an ultra-thin P3HT layer: a combined simulation and impedance spectroscopy study using experimental results", Journal of Optics, 2024. https://doi.org/10.1007/s12596-024-02324-9

[72] Ouslimane, T., Et-taya, L., Elmaimouni, L., Benami, A. "Impact of absorber layer thickness, defect density, and operating temperature on the performance of $MAPbI_3$ solar cells based on ZnO electron transporting material, Heliyon, 7(3), e06379, 2021. https://doi.org/10.1016/j.heliyon.2021.e06379

[73] Hossain, M. S., Amin, N., Matin, M. A., Aliyu, M. M., Razykov, T. M., Sopian, K. B. "A numerical study on the prospects of high efficiency ultra thin $Zn_xCd_{1-x}S$/CdTe solar cell", Chalcogenide Letters, 8(4), pp. 263–272, 2011.

[74] Chowdhury, T. A. "SCAPS modeling and performance analysis of AZO/SnS_2/CZTS solar cells", Optics Continuum, 3(8), pp. 1341–1368, 2024. https://doi.org/10.1364/OPTCON.527415

[75] Roshi, Singh, B., Gupta, V. "Modelling and simulation of silicon solar cells using PC1D", Materials Today: Proceedings, 54, pp. 810–813, 2022. https://doi.org/10.1016/j.matpr.2021.11.092

[76] Yu, X., Shi, Y., Yu, X., Zhang, J., Ge, Y., Chen, L., Pan, H. "Al-doping effects on the photovoltaic performance of inverted polymer solar cells", Optoelectronics Letters, 12(2), pp. 106–109, 2016. https://doi.org/10.1007/s11801-016-6003-8

[77] Dris, K., Benhaliliba, M. "Novel Inorganic–Organic Heterojunction Solar Cell-Based Perovskite Using Two Absorbent Materials", Nano, 18(11), 2350091, 2023. https://doi.org/10.1142/S1793292023500911

[78] Dris, K., Benhaliliba, M., Ayeshamariam, A., Roy, A., Kaviyarasu, K. "Improving the perovskite solar cell by insertion of methyl ammonium tin oxide and cesium tin chloride as absorber layers: scaps 1d study based on experimental studies", Journal of Optics, 2024. https://doi.org/10.1007/s12596-024-01996-7

[79] Dris, K., Benhaliliba, M. "Study and Optimization of a New Perovskite Solar Cell Structure Based on the Two Absorber Materials Cs_2TiBr_6 and $MASnBr_3$ Using SCAPS 1D", Periodica Polytechnica Chemical Engineering, 68(3), pp. 348–363, 2024. https://doi.org/10.3311/PPch.36825